



HAL
open science

Dynamics of rising bubble population undergoing mass transfer and coalescence in highly viscous liquid

Franck Pigeonneau, L. Pereira, A. Laplace

► **To cite this version:**

Franck Pigeonneau, L. Pereira, A. Laplace. Dynamics of rising bubble population undergoing mass transfer and coalescence in highly viscous liquid. *Chemical Engineering Journal*, 2022, pp.140920. 10.1016/j.cej.2022.140920 . hal-03903277

HAL Id: hal-03903277

<https://minesparis-psl.hal.science/hal-03903277>

Submitted on 16 Dec 2022

HAL is a multi-disciplinary open access archive for the deposit and dissemination of scientific research documents, whether they are published or not. The documents may come from teaching and research institutions in France or abroad, or from public or private research centers.

L'archive ouverte pluridisciplinaire **HAL**, est destinée au dépôt et à la diffusion de documents scientifiques de niveau recherche, publiés ou non, émanant des établissements d'enseignement et de recherche français ou étrangers, des laboratoires publics ou privés.

1 Dynamics of rising bubble population undergoing mass
2 transfer and coalescence in highly viscous liquid

3 F. Pigeonneau^a, L. Pereira^b, A. Laplace^c

4 ^a*MINES Paris, PSL Research University, CEMEF - Centre for material forming, CNRS UMR 7635,*
5 *CS 10207, rue Claude Daunesse 06904 Sophia Antipolis Cedex, France*

6 ^b*Ludwig-Maximilians-Universität München, Department of Earth and Environmental Sciences,*
7 *Theresienstraße 41, 80333 Munich, Germany*

8 ^c*CEA, DES, ISEC, DE2D, University of Montpellier, Marcoule, France*

9 **Abstract**

10 The two-phase flow dynamics involving mass transfer and coalescence is investigated.
11 The model is specifically developed to describe the dynamics of bubble population dis-
12 persed in glass forming liquids. The amounts of gas dissolved in the liquid are determined
13 using the chemical equilibrium involving oxidation-reduction reactions. The gravitational
14 bubble rising is used to write the coalescence kernel for which a collision efficiency is also
15 introduced.

16 Based on a Direct Quadrature Method of Moments (DQMOM), a numerical method is
17 developed. This numerical tool is applied to melting of borosilicate glass beads for which
18 temperature and residence time of the sample in a crucible are investigated. The bubble
19 density decreases sharply at short times. This early stage decrease is well explained and
20 quantified when the coalescence is taken into account in numerical computations. The
21 bubble size density is very well described with a log-normal distribution. Using the first
22 three moments, the bubble size distribution obtained numerically is in good agreement
23 with experimental data.

24 Numerical computations are also applied to soda-lime-silica glass in which the bubble
25 release is driven by the mass transfer between the two phases. The faster decrease of
26 bubble density than would be expected by temperature is reproduced by the numerical
27 computation. The enhancement of the bubble release rate is mainly due to the increase
28 of dissolved gas species with temperature.

29 *Keywords:* Population balance equation; glass forming liquid; coalescence; mass
30 transfer; method of moments

*Corresponding author: Tel. +33 (4) 93 95 74 34.

Email address: franck.pigeonneau@minesparis.psl.eu (F. Pigeonneau)

Preprint submitted to Chem. Eng. J.

December 13, 2022

31 **1. Introduction**

32 Multiphase and in particular bubbly flows are present in geophysics with the out-
33 gassing of volcanoes [1], in agribusiness industry with sparkling wines [2], in metallurgy
34 in which bubbles are used to stir molten metal or enhance the heat and mass transfer
35 [3], in power plants with boiling water in nuclear reactors [4], among others. Here, in-
36 vestigations are focused in glass melting process in which outgassing process is a major
37 phenomena leading to strong limitations in industrial plants. Understanding how bubbles
38 appear, disappear, interact, grow remains fundamental and applied issues.

39 In glass melting process, the bubble generation occurs mainly during the melting
40 of raw materials. As generally accepted, bubbles are created due to the trapping of
41 atmospheric gases and the decomposition of mineral species used as batch components
42 [5]. As already shown long time ago by one of a first contribution devoted to fining
43 process (impurity release) [6], the bubble release is mainly driven by the temperature.
44 Recent experiments of glass cullet melting in a small crucible confirm this assertion [7, 8].
45 Pereira et al. [8] pinpointed that the bubble dynamics (bubble density, mean radius)
46 can be rescaled by the residence time of a bubble in the bath directly linked to the
47 temperature via the dynamical viscosity. Cable [9] underlined that bubble coalescence
48 can play a role in the dynamics in the early stages of the process. In the review paper,
49 Cable [10] pointed out the “*rate of refining, [i.e. rate of bubble release,] varies more*
50 *with temperature than would be expected from the effects of temperature on bubble size*
51 *and viscosity*”. Predict the dynamics of bubble population undergoing gravitational
52 rising, mass transfer and coalescence is a task not completely fulfilled. Consequently, the
53 main purpose of this article is to study bubble populations rising in glass forming liquid
54 undergoing mass transfer and coalescence.

55 Describe the dynamics of a population undergoing processes such as mass transfer
56 and coalescence needs a model based on the population balance equation developed
57 long time ago by Randolph and Larson [11] and Hulburt and Katz [12]. Today, this
58 theory becomes primordial to study dispersed media. This theory has been presented
59 by Ramkrishna [13] for a large range of applications. Despite these contributions, the
60 theory was mainly limited to spatial homogeneous problems. A new step was overcome
61 with the major contribution of Marchisio and Fox [14] in which the theory and numerical
62 methods are applied to spatial inhomogeneous cases allowing the introduction of such
63 theory in Computational Fluid Dynamics software.

64 In the context of glass science, the population balance theory has been initially pro-
65 posed by Ungan et al. [15] to study the bubble density and the momentum coupling with
66 the carrier phase. Nevertheless, the chemical process is completely ignored. Ungan et
67 al. [16] investigated the silica grain dissolution in a glass bath with the same approach.

68 Roi et al. [17] developed a model to describe the bubble removal using a population
69 balance equation with only mass transfer process. Balkanli and Ungan [18] improved the
70 previous model by introducing a description of the bubble size distribution and the mass
71 transfer with only one species (CO_2). Bensberg and Breitbach [19] described the bubble
72 population assuming a predefined bubble size distribution corresponding to a log-normal
73 distribution and further solved the equations of first three moments to characterize the
74 bubble size distribution. Only one gas species is considered and the coupling is limited
75 to the momentum balance. Pilon et al. [20] proposed a population balance equation in
76 which the general aspect of the glass chemistry is described. The chemical reaction of
77 fining agents is seen as an irreversible chemical reaction. Pilon and Viskanta [21] applied
78 the previous model on the modeling of a glass furnace limiting to two gas species using
79 a modified characteristic method to solve the population balance equation [22] without
80 coalescence. Finally, Oda and Kaminoyama [23] studied the fining process coupling with
81 the bubble density conservation in two dimensional geometry.

82 Despite these contributions, the development of the population balance equation tak-
83 ing into account mass transfer and coalescence in glass melting process is not yet provided.
84 This is the main purpose of this contribution which is an extended version of the theoret-
85 ical model developed in [24]. First, problem statement is detailed in section 2 in which
86 mass transfer and coalescence processes are presented. The direct quadrature method
87 of moments (DQMOM) is described in section 3. Numerical computations detailed in
88 section 4 are based on experimental observations done in [8, 6]. Few conclusions are
89 finally drawn in section 5. Appendix A provides numerical data needed to achieve the
90 numerical computations.

91 2. Problem statement

92 2.1. Bubble state in phase space

93 The overall dynamics of a bubble population dispersed in a glass forming liquid in-
94 volves mass transfer between the dispersed and continuous phases, coalescence among
95 others. According to Ramos [25], and Pigeonneau [26], a bubble is composed by various
96 gas species coming from the atmosphere above the glass bath, and from the liquid itself.
97 Typically, gas species such as CO_2 , N_2 , H_2O , O_2 and SO_2 are involved. According to
98 Hulburt and Katz [12], the dynamics of a dispersed phase depends on external coordi-
99 nates corresponding to the spacial position where inclusions are localized and internal
100 coordinates characterizing the state of each particle. In the following, the temperature
101 is assumed uniform and constant in time.

102 Using the general drag force acting on a bubble [27, 28], the time scale required to
103 reach the steady-state regime is proportional to a^2/ν with a the bubble radius and ν

104 the kinematic viscosity of the liquid. The typical radius is around tens of micrometres
105 and the kinematic viscosity is around $10^{-2} \text{ m}^2/\text{s}$ [8]. Consequently, a^2/ν is order of
106 magnitude of 10^{-9} s sufficiently small to neglect the bubble inertia. The bubble velocity
107 is then removed from the internal coordinates since it can be explicitly determined. The
108 relative bubble velocity is given by the terminal rising velocity according to Hadamard
109 [29] and Rybczynski [30].

110 In principle, the rate of variation of the bubble radius requires the writing of the
111 Rayleigh-Plesset equation [31] given by

$$\rho \left[a\ddot{a} + \frac{3}{2}\dot{a}^2 \right] = P - P_0 - \frac{2\gamma}{a} - \frac{4\eta}{a}\dot{a}, \quad (1)$$

112 with ρ the density of the liquid, P the pressure inside the bubble and P_0 the pressure in
113 the liquid without the hydrostatic contribution, γ the surface tension and η the dynamic
114 viscosity.

115 The normalization of the Rayleigh-Plesset equation with the atmospheric pressure
116 leads to the inertia time scale of bubble variation equal to $a\sqrt{\rho/P_0}$. Moreover, the time
117 scale of the viscosity term is given by η/P_0 . These two characteristic times are around
118 10^{-6} to 10^{-5} s . Since the time scale due to the bubble rising over a distance equal to the
119 bubble radius, $\nu/(ga)$, is larger than 10s and the time scale of the mass transfer is in
120 general much larger than the rising time, a quasi-static state can be used to determine
121 the bubble pressure.

122 As already done by Pilon et al. [20], the molar fractions are considered as internal
123 coordinates to take into account the multi-component bubble composition. External
124 coordinates are \mathbf{r} , i.e. the position in space. Internal variables are bubble radius a and
125 the molar fractions $x_{g,i}$ with $i = 1$ to $N_g - 1$ and N_g the number of the gas species.
126 Recall that the sum of the molar fractions over index i is equal to one. According to
127 Pigeonneau [26], the rate of variation of \mathbf{r} , a and $x_{g,i}$ are

$$\mathbf{v} = \mathbf{u} - \frac{\mathbf{g}a^2}{3\nu}, \quad (2)$$

$$\dot{a} = \frac{1}{2a} \sum_{i=1}^{N_g} \text{Sh}(\text{Pe}_i) \mathcal{H}_i \mathcal{D}_i (x_{l,i} - x_{g,i}), \quad (3)$$

$$\dot{x}_{g,i} = \frac{3}{2a^2} \sum_{j=1}^{N_g} \text{Sh}(\text{Pe}_j) \mathcal{H}_j \mathcal{D}_j (\delta_{ij} - x_{g,i}) (x_{l,j} - x_{g,j}), \quad \forall i = [1; N_g - 1]. \quad (4)$$

128 In this system of equations, t is the time, \mathbf{u} the velocity field of the continuous phase,
129 \mathbf{g} the gravity field, ν is the kinematic viscosity. In the growth rate of a , eq. (3), Sh is

130 the Sherwood number depending on the Péclet number given by

$$\text{Pe}_i = \frac{2ga^3}{3\nu\mathcal{D}_i}. \quad (5)$$

131 In the creeping flow, the Sherwood number is strongly linked to the mobility of the
 132 bubble/liquid interface [32, 33]. While for immobile interface, the Sherwood number
 133 scales as $\sqrt[3]{\text{Pe}}$, Sh is proportional to $\sqrt{\text{Pe}}$ for mobile interface in the limit of high Péclet
 134 number. According to Pigeonneau et al. [34], the study on the shrinkage of O₂ bubble in
 135 glass forming liquid shows that the bubble/liquid interface can be considered as mobile.
 136 Consequently, the Sherwood number is determined by the correlation proposed by Clift
 137 et al. [33] equal to

$$\text{Sh}(\text{Pe}) = 1 + \left(1 + 0.564\text{Pe}^{2/3}\right)^{3/4}. \quad (6)$$

138 The quantity \mathcal{H}_i is the dimensionless solubility given as a function of the Henry
 139 coefficient

$$\mathcal{L}_i = \frac{C_i^s}{P_i} \quad (7)$$

140 by [35]

$$\mathcal{H}_i = RT\mathcal{L}_i, \quad (8)$$

141 with R the perfect gas constant and T the temperature in K. In eq. (7), C_i^s is the
 142 molar concentration at the interface between the liquid and the atmosphere in which the
 143 gas species has a partial pressure equal to P_i . In eqs. (3) and (4), \mathcal{D}_i is the diffusion
 144 coefficient of the species i in the liquid. The dimensionless variable $x_{l,i}$ corresponds to
 145 the gas saturation in the liquid of the i species defined by

$$x_{l,i} = \frac{C_i^l}{\mathcal{L}_i P}, \quad (9)$$

146 in which C_i^l is the molar concentration of the gas species dissolved in the liquid. According
 147 to Pigeonneau [26], the effects of the hydrostatic and Laplace pressures can be neglected.
 148 The total pressure in each bubble P is assumed equal to the atmospheric pressure above
 149 the liquid bath.

150 2.2. Population balance equation

151 Integration of equations (2-4) associated with initial conditions gives a particular
 152 trajectory in the phase space $(\mathbf{r}, a, \mathbf{x}_g)$ with $\mathbf{x}_g = (x_{g,1}, \dots, x_{g,N_g-1})$. Applied to a large
 153 number of bubbles, a density function can be defined in the limit of the large number
 154 of particles written $f(\mathbf{r}, t; a, \mathbf{x}_g)$ in which by convention the Eulerian variables (\mathbf{r}, t) has
 155 been separated by a semicolon of the internal coordinates. This function is assumed

156 sufficiently smooth to be differentiable [14]. From this definition $f(\mathbf{r}, t; a, \mathbf{x}_g) d\mathbf{r} da d\mathbf{x}_g$ is
 157 the number of inclusions in an elementary hyper-volume embodied between \mathbf{r} and $\mathbf{r} + d\mathbf{r}$,
 158 a and $a + da$, \mathbf{x}_g and $\mathbf{x}_g + d\mathbf{x}_g$. According to Ramkrishna [13] and Marchisio and Fox
 159 [14], the balance equation of population is given by

$$\frac{\partial f}{\partial t} + \nabla \cdot (\mathbf{v}f) + \frac{\partial(\dot{a}f)}{\partial a} + \sum_{i=1}^{N_g-1} \frac{\partial(\dot{x}_{g,i}f)}{\partial x_{g,i}} = h(\mathbf{r}, t; a, \mathbf{x}_g), \quad (10)$$

160 in which \mathbf{v} , \dot{a} and $\dot{x}_{g,i}$ are the right-hand side of eqs. (2-4) respectively and h is a source
 161 term resulting of the birth and the death of bubbles due to coalescence, breakup or
 162 nucleation.

163 The mass transfer between the bubble population changes the amount of dissolved
 164 gas in the liquid which can be introduced in molar conservation of the gas species i as
 165 follows

$$\frac{\partial x_{l,i}}{\partial t} + \nabla \cdot (\mathbf{u}x_{l,i}) = \mathcal{D}_i \nabla^2 x_{l,i} - 2\pi \int_0^\infty \int_{\Omega_{\mathbf{x}_g}} a \text{Sh}(\text{Pe}_i) \mathcal{D}_i(x_{l,i} - x_{g,i}) f(\mathbf{r}, t; a, \mathbf{x}_g) d\mathbf{x}_g da, \quad (11)$$

166 for all $i \in [1, N_g]$. The domain $\Omega_{\mathbf{x}_g}$ in the space \mathbf{x}_g is equal to $[0, 1]^{N_g-1}$.

167 To solve the population balance equation, a size-conditioned density is defined as
 168 follows [36, 14]

$$n(\mathbf{r}, t; a) = \int_{\Omega_{\mathbf{x}_g}} f(\mathbf{r}, t; a, \mathbf{x}_g) d\mathbf{x}_g, \quad (12)$$

169 and a size-conditioned of a quantity G is then defined by

$$\langle G|a \rangle = \frac{\int_{\Omega_{\mathbf{x}_g}} G f(\mathbf{r}, t; a, \mathbf{x}_g) d\mathbf{x}_g}{n(\mathbf{r}, t; a)}. \quad (13)$$

170 The moment of the k order is given by

$$\mu_k(\mathbf{r}, t) = \int_0^\infty a^k n(\mathbf{r}, t; a) da. \quad (14)$$

171 The zeroth order moment is simply the bubble density. The second order moment is propo-
 172 portional to the interfacial area concentration and the third order moment is proportional
 173 to the volume fraction of bubble.

174 The population balance equation applied to $n(\mathbf{r}, t; a)$ is then given by

$$\frac{\partial n}{\partial t} + \nabla \cdot (\langle \mathbf{v}|a \rangle n) + \frac{\partial(\langle \dot{a}|a \rangle n)}{\partial a} = S(\mathbf{r}, t; a), \quad (15)$$

175 after integration over the total space of molar fractions with $S(\mathbf{r}, t; a)$ the integral of
 176 $h(\mathbf{r}, t; a, \mathbf{x}_g)$. Equation on the gas saturation becomes

$$\frac{\partial x_{l,i}}{\partial t} + \nabla \cdot (\mathbf{u}x_{l,i}) = \mathcal{D}_i \nabla^2 x_{l,i} - 2\pi \int_0^\infty a \text{Sh}(\text{Pe}_i) \mathcal{D}_i(x_{l,i} - \langle x_{g,i} | a \rangle) n(\mathbf{r}, t; a) da. \quad (16)$$

177 *2.3. Coalescence source term*

178 The release of bubbles in a molten glass is mainly driven by the buoyancy force. Due
 179 to large initial bubble density, collision and coalescence are strongly likely to happen.
 180 The source term $S(\mathbf{r}, t; a)$ due to the coalescence process is equal to [14]

$$S(\mathbf{r}, t; a) = \frac{1}{2} \int_0^a \frac{a^2}{(a^3 - a'^3)^{2/3}} K(a', \sqrt[3]{a^3 - a'^3}) n(\mathbf{r}, t; a') n(\mathbf{r}, t; \sqrt[3]{a^3 - a'^3}) da' - \\ n(\mathbf{r}, t; a) \int_0^\infty K(a, a') n(\mathbf{r}, t; a') da', \quad (17)$$

181 with $K(a, a')$ the coalescence kernel.

182 This quantity depends on the nature of the bubble motion and the kind of the flow,
 183 laminar or turbulent [37]. In the case of the bubble rising motion in creeping regime,
 184 $K(a, a')$ is written as follows [38]

$$K(a, a') = \frac{g\pi}{3\nu} (a + a')^2 |a^2 - a'^2| E_{\text{col}}(a, a'), \quad (18)$$

185 with $E_{\text{col}}(a, a')$ the collision efficiency. The physical meaning of this quantity is simply
 186 the ratio of the collision section due to hydrodynamic interactions divided by the collision
 187 section without interaction equal to $\pi(a + a')^2$ [39, 38]. According to these two previous
 188 contributions, the coalescence efficiency in the limit of spherical bubbles taking into
 189 account the hydrodynamic interaction does not change significantly with the bubble
 190 ratio a/a' and is roughly equal to 0.2.

191 **3. Direct quadrature method of moments**

192 Various numerical methods have been developed over the years to solve the popu-
 193 lation balance equation. A first class of methods is based on a discretization of the
 194 internal coordinate. This kind of method has been used to study the rain formation by
 195 Kovetz and Olund [40]. A same approach has been used to study droplet population in
 196 homogeneous isotropic turbulence [41]. Finite element and orthogonal collocation have
 197 been developed by Gelbard and Seinfeld [42]. Ramkrishna [43] developed a method of
 198 weighted residuals with Laguerre function as trial functions (see also [44]). In the context
 199 of glass melting process, Pilon and Viskanta [22] determined directly the density function

200 using a reverse characteristic method. Hulburt and Katz [12] proposed to solve equations
 201 on the moments of the density function. To close the system of equations the density
 202 function is written with Γ -distribution and associated Laguerre polynomials [45].

203 Here, the direct quadrature method of moments initially proposed by Marchisio and
 204 Fox [46] is used. This method enables to take into account the various processes such as
 205 bubble growth, coalescence, break-up and nucleation phenomena with a simple closure
 206 procedure.

207 3.1. Spatial inhomogeneous formulation

208 In method of moments, the density function $n(\mathbf{r}, t; a)$ is written as a summation of
 209 Dirac delta functions as follows [46]

$$n(\mathbf{r}, t; a) = \sum_{\alpha=1}^N \omega_{\alpha}(\mathbf{r}, t) \delta[a - a_{\alpha}(\mathbf{r}, t)], \quad (19)$$

210 in which $\omega_{\alpha}(\mathbf{r}, t)$ is the weight of integration of the node (abscissa) $a_{\alpha}(\mathbf{r}, t)$ and N
 211 corresponds to the number of classes representing the density function. The $2N$ first mo-
 212 ment equations are required to determine the N couples $(\omega_{\alpha}, a_{\alpha})$. Generally, a product-
 213 difference [47] or Wheeler algorithms [48] are used to find the weights and abscissas. It
 214 is well-known that this kind of method can be ill-posed if two abscissas become equal.

215 To circumvent this difficulty, Marchisio et al. [49] proposed an alternative method to
 216 determine directly the N couples $(\omega_{\alpha}, a_{\alpha})$. Before to detail the direct quadrature method
 217 of moments, a dimensionless form of (15) and (16) is written. Our main goal is to study
 218 the release of bubble population from a glass forming liquid in a crucible with a height
 219 H . According to Pereira et al. [8], the characteristic time is equal to $H\nu/(ga_0^2)$. The
 220 characteristic bubble radius a_0 is defined as follows

$$a_0 = \sqrt[3]{\frac{\mu_3}{\mu_0}}. \quad (20)$$

221 If N_0 is the initial bubble density in m^{-3} , the bubble density function $n(\mathbf{r}, t; a)$ is
 222 reduced by the ratio N_0/a_0 . The velocity field is normalized by ga_0^2/ν and spatial coordi-
 223 nates by H , the liquid height. For convenient reason, dimensionless variables are written
 224 with the same symbols used previously meaning that the population balance equation
 225 (15) does not change. Bubble growth rate and the coalescence kernel are modified as

226 follows

$$\langle \dot{a} | a \rangle = \frac{1}{2a} \sum_{i=1}^{N_g} \text{Sh}(\text{Pe}_i) \mathcal{H}_i \text{Fo}_i (x_{l,i} - \langle x_{g,i} | a \rangle), \quad (21)$$

$$K(a, a') = \frac{K_0 E_{\text{coa}}}{12} (a + a')^2 |a^2 - a'^2|, \quad (22)$$

227 in which Fo_i corresponding to a Fourier number and K_0 are given by

$$\text{Fo}_i = \frac{\nu H \mathcal{D}_i}{g a_0^4}, \quad (23)$$

$$K_0 = 4\pi N_0 a_0^2 H. \quad (24)$$

228 The rate of the size-conditioned molar fraction has to be written as follows

$$\langle \dot{x}_{g,i} | a \rangle = \frac{3}{2a^2} \sum_{j=1}^{N_g} \text{Sh}(\text{Pe}_j) \mathcal{H}_j \text{Fo}_j (\delta_{ij} - \langle x_{g,i} | a \rangle) (x_{l,j} - \langle x_{g,j} | a \rangle), \quad \forall i = [1; N_g - 1]. \quad (25)$$

229 Finally, the transport equation in the saturation of the gas species i takes the following
230 form

$$\frac{\partial x_{l,i}}{\partial t} + \nabla \cdot (\mathbf{u} x_{l,i}) = \frac{a_0^2 \text{Fo}_i}{H^2} \nabla^2 x_{l,i} - \frac{3\varphi_0}{2} \int_0^\infty a \text{Sh}(\text{Pe}_i) \text{Fo}_i (x_{l,i} - \langle x_{g,i} | a \rangle) n(\mathbf{r}, t; a) da, \quad (26)$$

231 with

$$\varphi_0 = \frac{4\pi a_0^3 N_0}{3}, \quad (27)$$

232 corresponding to the initial volume fraction of the bubble population. The coefficient
233 K_0 given by eq. (24) characterizes also the initial bubble population. It is equal to
234 the product of the interfacial area concentration by the crucible height. Physically, this
235 dimensionless group can be seen as the surface area ratio of the bubble population to
236 the free surface of the fluid domain. A large value of K_0 means that the coalescence is
237 important and the mass transfer is mainly between the bubble population and the liquid.

238 According to Marchisio and Fox [49], the transport equations of the N couples $(\omega_\alpha, a_\alpha)$
239 are obtained by introduction of (19) in the population balance equation (15) which gives

$$\frac{\partial \omega_\alpha}{\partial t} + \nabla \cdot (\mathbf{v}_\alpha \omega_\alpha) = A_\alpha, \quad (28)$$

$$\frac{\partial \zeta_\alpha}{\partial t} + \nabla \cdot (\mathbf{v}_\alpha \zeta_\alpha) = B_\alpha, \quad (29)$$

240 with $\zeta_\alpha = \omega_\alpha a_\alpha$ and $\mathbf{v}_\alpha = \langle \mathbf{v} | a_\alpha \rangle$. The $2N$ right-hand sides A_α and B_α are solution of

241 the linear system

$$(1 - k) \sum_{\alpha=1}^N a_{\alpha}^k A_{\alpha} + k \sum_{\alpha=1}^N a_{\alpha}^{k-1} B_{\alpha} = C_k, \quad \forall k \in [0; 2N], \quad (30)$$

242 and C_k is equal to

$$C_k = \sum_{\alpha=1}^N \sum_{\beta=1}^N \omega_{\alpha} \omega_{\beta} K(a_{\alpha}, a_{\beta}) \left[\frac{(a_{\alpha}^3 + a_{\beta}^3)^{k/3}}{2} - a_{\beta}^k \right] + k \sum_{\alpha=1}^N a_{\alpha}^{k-1} \dot{a}_{\alpha} \omega_{\alpha}, \quad (31)$$

243 with $\dot{a}_{\alpha} = \langle \dot{a} | a_{\alpha} \rangle$ given by eq. (21) with the bubble size equal to a_{α} .

244 To close the growth rate, the $N_g - 1$ molar fractions and for each bubble class α
 245 written as $\langle x_{g,i} | a_{\alpha} \rangle$ have to be solved using the following transport equation

$$\frac{\partial \langle x_{g,i} | a_{\alpha} \rangle}{\partial t} + \nabla \cdot (\mathbf{v}_{\alpha} \langle x_{g,i} | a_{\alpha} \rangle) = \frac{3}{2a_{\alpha}^2} \sum_{j=1}^{N_g} \text{Sh}(\text{Pe}_{j,\alpha}) \mathcal{H}_j \text{Fo}_j (\delta_{ij} - \langle x_{g,i} | a_{\alpha} \rangle) (x_{l,j} - \langle x_{g,j} | a_{\alpha} \rangle), \quad (32)$$

246 $\forall i = [1; N_g - 1]$. Quantity $\text{Pe}_{j,\alpha}$ is the Péclet number given by (5) based on the bubble
 247 size a_{α} . Finally the N_g gas saturations are solution of

$$\frac{\partial x_{l,i}}{\partial t} + \nabla \cdot (\mathbf{u} x_{l,i}) = \frac{a_0^2 \text{Fo}_i}{H^2} \nabla^2 x_{l,i} - \frac{3\varphi_0}{2} \sum_{\alpha=1}^N a_{\alpha} \omega_{\alpha} \text{Sh}(\text{Pe}_{i,\alpha}) \text{Fo}_i (x_{l,i} - \langle x_{g,i} | a_{\alpha} \rangle). \quad (33)$$

248 The total number of equations to solve the dispersed phase is equal to $2N + N(N_g - 1)$
 249 completed by the N_g transport equations on $x_{l,i}$. The system of equations is close to
 250 the previous one provided by Pigeonneau [24] to study the interaction between a bubble
 251 population and the chemistry of glass forming liquid without the interaction between
 252 bubble classes.

253 3.2. Spatial homogeneous formulation

254 The previous system of equations needs to be completed by the balance equations
 255 to determine the velocity and the pressure of the continuous phase. Since our main
 256 objective is to compare with experiments achieved in a crucible in which only volume
 257 averages data are known, only spatial homogeneous formulation is presented and solved
 258 in the following. To determine the volume average equations, the appropriate method is
 259 to first average the population balance equation which becomes

$$\frac{\partial \langle n \rangle}{\partial t} + \frac{\partial (\langle \dot{a} | a \rangle \langle n \rangle)}{\partial a} = \langle S \rangle(t; a) - \frac{\langle n \rangle a^2}{3}, \quad (34)$$

260 in which $\langle \rangle$ corresponds to the volume average. The extra sink term of the right-hand
 261 side of the previous equation represents the bubble release through the free surface of
 262 the glass bath. In this formulation, the mass interaction between the liquid and the
 263 atmosphere is neglected at the free surface of the domain. This assumption is justified
 264 when the K_0 product is larger than one. This will be fulfilled in the next section.

265 The development of the direct quadrature method of moments does not change. In
 266 this case, all quantities are averaged on the total volume of the domain. The ordinary
 267 differential equations are then the following

$$\frac{d\omega_\alpha}{dt} = A_\alpha, \forall \alpha \in [1, N], \quad (35)$$

$$\frac{d\zeta_\alpha}{dt} = B_\alpha, \forall \alpha \in [1, N], \quad (36)$$

$$\begin{aligned} \frac{d\langle x_{g,i}|a_\alpha \rangle}{dt} &= \frac{3}{2a_\alpha^2} \sum_{j=1}^{N_g} \text{Sh}(\text{Pe}_{j,\alpha}) \mathcal{H}_j \text{Fo}_j (\delta_{ij} - \langle x_{g,i}|a_\alpha \rangle) (x_{l,j} - \langle x_{g,j}|a_\alpha \rangle), \\ &\forall i \in [1, N_g - 1], \end{aligned} \quad (37)$$

$$\frac{dx_{l,i}}{dt} = -\frac{3\varphi_0}{2} \sum_{\alpha=1}^N a_\alpha \omega_\alpha \text{Sh}(\text{Pe}_{i,\alpha}) \text{Fo}_i (x_{l,i} - \langle x_{g,i}|a_\alpha \rangle), \forall i \in [1, N_g]. \quad (38)$$

268 The N couples (A_α, B_α) are always solution of (30) but C_k takes the following form

$$\begin{aligned} C_k &= \sum_{\alpha=1}^N \sum_{\beta=1}^N \omega_\alpha \omega_\beta K(a_\alpha, a_\beta) \left[\frac{(a_\alpha^3 + a_\beta^3)^{k/3}}{2} - a_\beta^k \right] + k \sum_{\alpha=1}^N a_\alpha^{k-1} \langle \dot{a}|a_\alpha \rangle \omega_\alpha \\ &\quad - \sum_{\alpha=1}^N \frac{\omega_\alpha a_\alpha^{k+2}}{3}, \end{aligned} \quad (39)$$

269 with $\langle \dot{a}|a_\alpha \rangle$ given by eq. (21) with the bubble size equal to a_α .

270 Initially, the bubble size distribution is imposed using results obtained in [8]. Using a
 271 Wheeler algorithm, weight and abscissa of the α class are determined at t equal zero. The
 272 system of ordinary differential equations, (35-38) completed by (39) and (21) is solved
 273 using a Runge-Kutta method at the fourth order. The software is accessible in the github
 274 platform, see the link given at the end of the article.

275 4. Results and discussion

276 4.1. Glass melting of borosilicate glass beads

277 To study experimentally the dynamics of the bubble in a glass forming liquid, glass
 278 powders are prepared from synthesized borosilicate glasses. The accurate composition

279 can be found in [8]. Sizes of the granular media are in the range of (250-500) μm .
 280 The glass powder is introduced in a cylindrical alumina crucible with an inner diameter
 281 equal to 28 mm and a height equal to 40 mm. The density of the glass forming liquid is
 282 taken equal to 2270 kg/m^3 [50]. The dynamic viscosity is a function of the temperature
 283 determined from the Vogel-Fulcher-Tammann's law [51] as follows

$$\eta(T) = 8.39 \cdot 10^{-3} \exp\left(\frac{6026.88}{T - 610.16}\right), \quad (40)$$

284 with T in Kelvin. The glass transition temperature is found equal to 523 $^{\circ}\text{C}$ and
 285 the softening (Littleton) temperature is equal to 637 $^{\circ}\text{C}$. The former is defined for
 286 $\eta(T_g)=10^{12}$ Pa.s, while the latter for $\eta(T_s) = 10^{6.65}$ Pa.s [52]. The Littleton tempera-
 287 ture corresponds to the value above which the media collapses under its own weight.

288 After filling, each crucible is introduced in a furnace controlled in temperature during
 289 a certain time. When the desired residence time is over, the crucible is removed from
 290 the furnace to be cooled down until the room temperature. Each crucible is cut from
 291 the middle. One half is mounted in epoxy resin and then polished for optical microscope
 292 imaging. Figure 1 presents binarized optical microscope images obtained for T equal to
 293 1000 and 1100 $^{\circ}\text{C}$. Three melting times are shown at 20, 40, and 60 min. At 20 min and
 294 1000 $^{\circ}\text{C}$, the sample has a large population of small bubbles in comparison to the sample
 295 at the same melting time but at 1100 $^{\circ}\text{C}$. For longer times at 1000 $^{\circ}\text{C}$, samples show
 296 that the bubble population stays relatively elevated. Heterogeneity is clearly visible in
 297 Figure 1. Large bubbles are observed close to the crucible walls. The largest bubbles are
 298 mainly localized close to the vertical boundaries of the crucible and to the free surface.
 299 For T equal to 1100 $^{\circ}\text{C}$, the bubble population decreases strongly with time. A large
 300 fraction of tiny bubbles in the two bottom corners is observed for T equal to 1100 $^{\circ}\text{C}$ and
 301 a residence time of 60 min. Remark that the free surface are strongly curved while it is
 302 not expected at a temperature larger than T_s [7]. This effect comes from the thermal
 303 cooling leading to a thermal contraction of the gas phase and also a shrinkage due to the
 304 glass transition temperature.

305 From the binarized optical microscope images, an analysis is done to determine the
 306 bubble numbers by surface unit, the surface fraction and average size over the time. A
 307 detailed presentation has been already published in [8]. Since the theoretical model has
 308 been developed for a 3D configuration, the 2D data obtained by image analysis from the
 309 cut views depicted in Figure 1 must be converted in 3D data. To do so, the general
 310 principle of the stereology [53] is used. Mainly, the equality between the surface fraction
 311 and volume fraction is used to determine the bubble volume density. Since the bubble
 312 dimensions are determined at room temperature, a correction is applied to estimate the

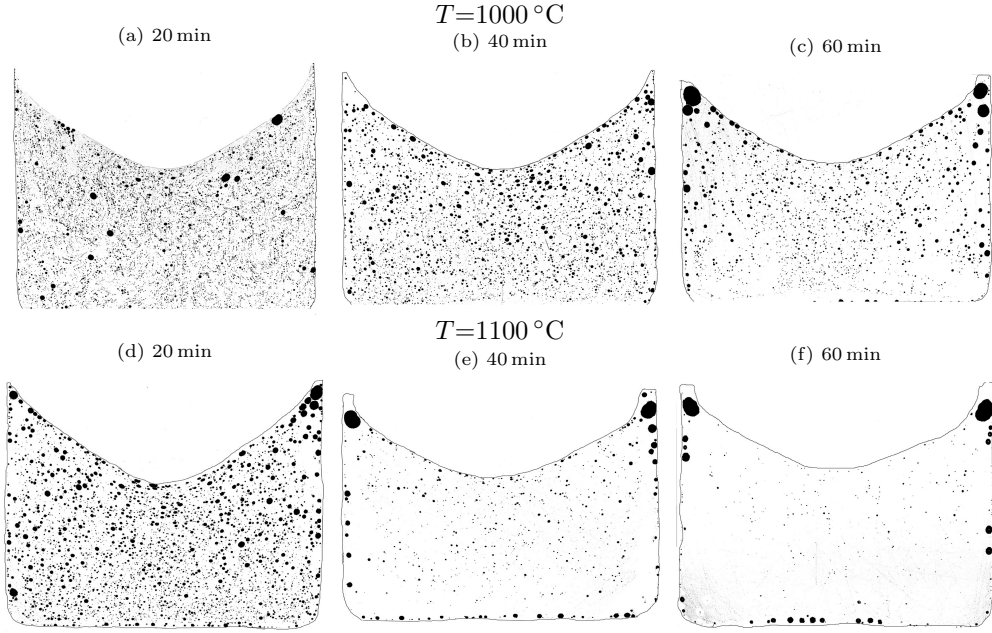


Figure 1: Binarized optical microscope images of samples for two temperatures and three melting times.

313 bubble size and volume at the temperature T . The glass forming liquid behaves like a
 314 solid when the temperature becomes smaller than the softening temperature, T_s . The
 315 volume correction is determined by multiplying the bubble volume at room temperature
 316 by a factor T/T_s . For the radius, the factor is $\sqrt[3]{T/T_s}$.

317 The initial conditions for the numerical computations are taken from the experimental
 318 data for the smallest residence time, i.e. 20 min. The relevant parameters for T equal
 319 to 1000, 1050 and 1100 °C are reported in Table 1. The initial bubble density is a huge
 320 quantity of bubbles since in a volume of one cubic millimeter, the number of bubbles
 321 reaches more than few hundreds. This relative large amount of bubbles is related to a
 322 small granulometry of the initial glass beads as seen by Boloré et al. [7]. It is important
 323 to stress that the volume fraction is small in comparison of the expected value in the
 324 original granular media. Due to the collapse of glass beads during the heating, large
 325 quantity of the gas phase are removed from the liquid [7]. Consequently, the height of
 326 the liquid is roughly reduced by a factor two. Even if the crucible is fully filled of granular
 327 media at room temperature, the height of liquid during the residence of the crucible in
 328 the furnace is taken equal to one-half of the crucible height, i.e. 20 mm. For the three
 329 temperatures, the values of K_0 are always larger than one meaning that the coalescence
 330 is expected to be the most relevant phenomena. As already pointed out above, the K_0
 331 product is the area ratio of the bubble population to the free surface of the crucible. This

Table 1: Initial bubble density, φ_0 and K_0 used in the numerical computation for three temperatures.

T ($^{\circ}\text{C}$)	N_0 (m^{-3})	φ_0	K_0
1000	3.45×10^{11}	1.21×10^{-1}	165.96
1050	1.90×10^{11}	1.47×10^{-1}	155.00
1100	6.88×10^{10}	1.68×10^{-1}	121.00

Table 2: Parameters μ and σ of the log-normal distribution, eq. (41) for the three temperatures.

T ($^{\circ}\text{C}$)	μ	σ
1000	3.34	0.54
1050	3.57	0.56
1100	3.72	0.68

332 means that the surface exchange is roughly around one hundred more efficient through
 333 the bubble surface than from the free surface.

334 Bubble size distributions are determined from images taken at 20 min. The proba-
 335 bility density functions under histogram form and for each temperature are depicted in
 336 Figure 2. Due to a limit of the bubble detection, there is no bubbles for radius smaller
 337 than $15 \mu\text{m}$. The bubble size distribution is more and more spread when the tempera-
 338 ture increases. As already found in [7], the bubble size distribution is well described by
 339 a log-normal distribution written as follows

$$f(a, \mu, \sigma) = \frac{1}{a\sigma\sqrt{2\pi}} \exp\left[-\frac{(\ln a - \mu)^2}{2\sigma^2}\right]. \quad (41)$$

340 The two dimensionless coefficients, μ and σ are computed from the mean radius and the
 341 variance of experimental data. The numerical values are reported in Table 2 for a size
 342 bubble distribution determined in μm^{-1} .

343 Solid lines in Figure 2 are the log-normal distributions using the data of Table 2. As
 344 underlined in [7], the bubble density function is well described by a log-normal distribu-
 345 tion because the void in the initial granular material follows a log-normal distribution as
 346 shown by Reboul et al. [54].

347 In the following, numerical computations are achieved with N equal to 3. The log-
 348 normal distribution obtained at each temperature is used to determine the initial values
 349 of a_α and ω_α by the Wheeler algorithm for α equal from 1 to 3. Since each couple
 350 $(a_\alpha, \omega_\alpha)$ is a Dirac representation of the bubble distribution, Figure 2 provides also the
 351 two first couples $(a_\alpha, \omega_\alpha)$. The two first classes exhibit the largest magnitude centered
 352 in the range of radius where the probability density function is important. For both
 353 temperature, the weight of the last class is very small and the respective abscissa is out
 354 of the range of the x axis of Figure 2.

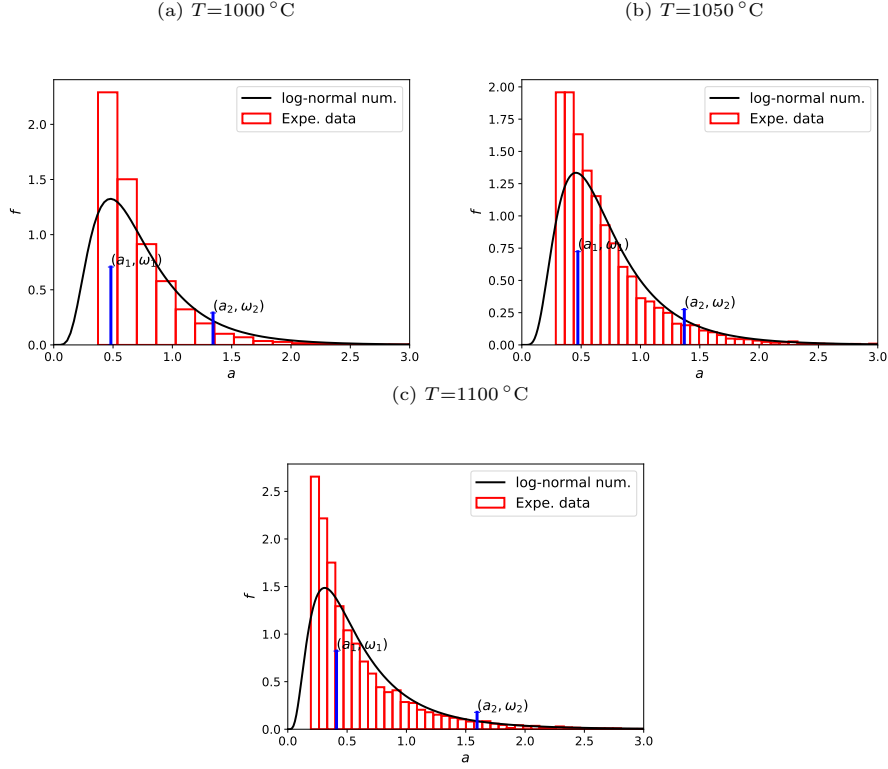
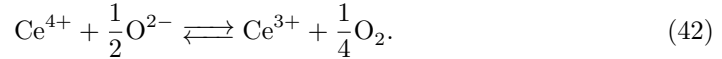


Figure 2: Initial normalized probability density function as a function of a determined from image analysis for the three temperatures at 20 min. Log-normal distribution and the amplitudes of initial ω_{α} are also reported for α equal 1 and 2.

355 From these data, numerical computations solving the problem presented in the pre-
356 vious section have been done for the three temperatures of the experiment. Three gas
357 species are considered: O_2 , N_2 and CO_2 . Since the bubble formation is mainly due
358 to the collapse of the liquid when the temperature becomes larger than the softening
359 temperature, the initial composition of bubbles is taken close to the air composition.
360 According to Pereira et al. [8], the molar fractions of O_2 , N_2 and CO_2 are initially taken
361 equal to 0.2, 0.7 and 0.1 respectively. Solubilities and diffusion coefficients are gathered
362 in [Appendix A](#). The concentrations of dissolved gas in the liquid has been determined
363 using the oxidation-reduction reaction of cerium given by



364 The equilibrium constant of this reaction is given by

$$K_{\text{Ce}} = \frac{C_{\text{Ce}^{3+}}^l \sqrt[4]{C_{\text{O}_2}^l}}{C_{\text{Ce}^{4+}}^l} = \exp\left(-\frac{\Delta G_{\text{Ce}}}{RT}\right), \quad (43)$$

365 with $C_{\text{Ce}^{4+}}^l$, $C_{\text{Ce}^{3+}}^l$ the molar concentration of Ce^{4+} and Ce^{3+} in the liquid. The Gibbs
366 energy is written as follows

$$\Delta G_{\text{Ce}} = \Delta H_{\text{Ce}} - T\Delta S_{\text{Ce}}. \quad (44)$$

367 The enthalpy and entropy of the reaction (42) has been determined by Pinet et al. [55]
368 and are given in Appendix A. Nitrogen and carbon oxide have a molar concentrations
369 equal to 10^{-2} mol/m^3 and $4 \times 10^{-2} \text{ mol/m}^3$ respectively. Data needed to compute solu-
370 bilities and diffusion coefficients are given in Appendix A.

371 To measure the relevance of the coalescence phenomena, numerical simulations have
372 been done with and without the coalescence source term. Figure 3 depicts the zeroth
373 order moment corresponding to the bubble density as a function of the normalized time.
374 This quantity is normalized by the initial bubble density. The solid line is the result
375 obtained with coalescence and the dashed line without coalescence. Black dots are the
376 experimental data.

377 While without coalescence source term, μ_0 decreases slowly due to the release of the
378 bubble from the crucible, the behavior changes dramatically when the coalescence is
379 accounted for. A fast decrease of the bubble density is observed at short experimental
380 durations. This first stage is followed by a small decrease of bubble as a function of
381 time. This general behavior is found regardless of temperature. Numerical computations
382 achieved with coalescence reproduce very well the experimental observations. In the early
383 stages, the coalescence is the main phenomena involved in the bubble dynamics rising in
384 the glass forming liquid as proposed by Cable [9]. The coalescence efficiency has been
385 taken equal to 0.175 to obtain the best comparison for the three temperatures.

386 With the decrease of the bubble density, coalescence events are scarcer and scarcer
387 since the source term of the coalescence is proportional to the square of the probability
388 density function. These numerical results justify also to consider a coalescence kernel
389 due to the bubble rising. The coalescence becomes negligible when the zeroth moment
390 decrease of one order of magnitude. The relevance of the coalescence is measured by the
391 magnitude of K_0 given by eq. (24). As reported in Table 1, the value of K_0 computed
392 with the bubble densities at the smallest residence time in the crucible is order to few
393 tens. With a decrease of the bubble density of one order of magnitude, the importance of
394 the coalescence becomes relevant when K_0 is larger than one. The bubble density should

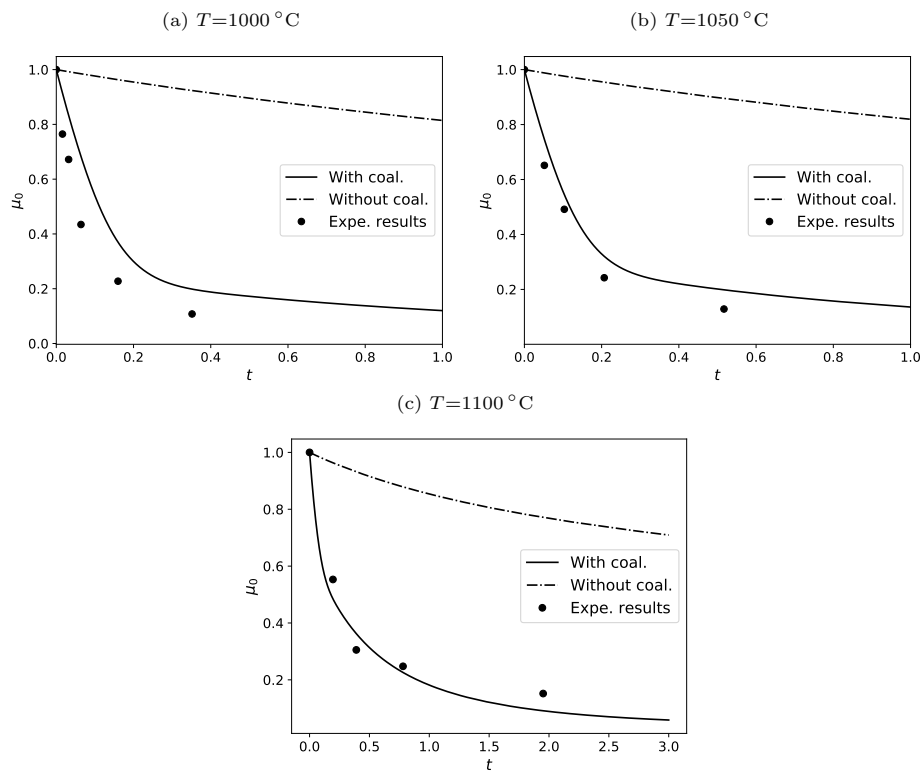


Figure 3: μ_0 as a function of t obtained numerically with and without coalescence and experimentally for three temperatures.

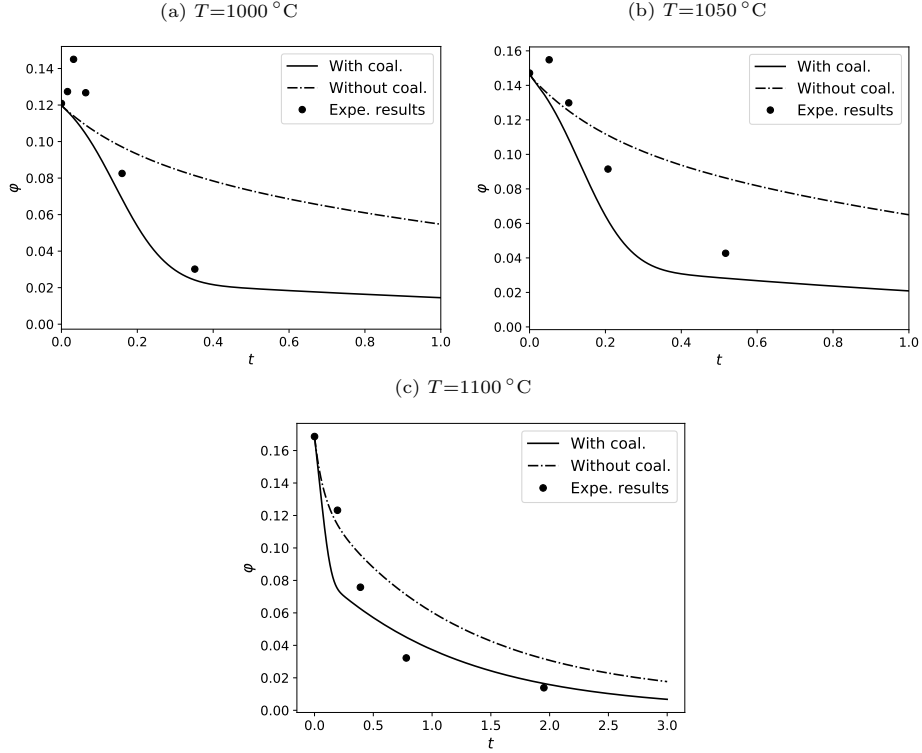


Figure 4: $\varphi = 4\pi\mu_3/3$ as a function of t obtained numerically with and without coalescence and experimentally for three temperatures.

395 be larger than 10^2 cm^{-3} to have a significant effect of the coalescence. In other words,
 396 the probability of coalescence is mainly linked to distance between two bubbles. Since
 397 the distance separating two bubbles is proportional to $1/\sqrt[3]{N_0}$ [56], the probability of
 398 coalescence becomes relevant when the distance between two bubbles is less than 1 mm.

399 Figure 4 presents the behavior of the volume fraction as a function of normalized
 400 time. Once again, the effect of the coalescence is clear. The comparison with experimental
 401 results is less satisfying. The unexpected increase of volume fraction at short times is due
 402 to an experimental artifact. Bubbles with a size smaller than the detection threshold
 403 are not taken into account in the volume fraction at short times. Due to the bubble
 404 dynamics, these tiny bubbles become enough large to be detected for larger residence
 405 times. This artifact disappears for T equal to 1100°C . It is mainly due to the faster
 406 bubble dynamics leading to observation of tiny bubbles at the first residence times. Apart
 407 from this beginning, experiments exhibits a strong decrease of the volume fraction with
 408 a rate close to this one determined numerically.

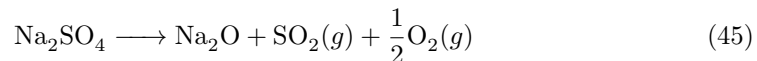
409 The probability density functions after 2 h in the furnace are determined from ex-

410 perimental data. Numerical results are used to determine the bubble size distribution
 411 following a log-normal distribution. The three first moments of numerical solutions are
 412 needed to determine μ and σ of eq. (41). The zeroth moment is required to renormalize
 413 ω_α . The first and second moments allow to determine the mean and the standard devi-
 414 ation of the bubble size distribution. Figure 5 depicts the probability density function
 415 under histogram form obtained from image analysis for the three temperatures after a
 416 residence time in the furnace of 120 min. The log-normal distributions obtained from the
 417 numerical values of the first three moments are also plotted in solid line. The amplitude
 418 and position of each class are also provided. The comparison between experimental and
 419 numerical distributions is very good for the two first temperatures. For $T=1100^\circ\text{C}$, an
 420 over-representation in the smallest radius is observed. This large source of tiny bubbles
 421 is the result of the observation of Figure 1(f). This source of tiny bubbles could be an
 422 artificial bubble creation due to the post-morten treatment. It is particularly observed
 423 at this temperature and time because the total of bubbles are the smallest. Nevertheless,
 424 the decrease of the distribution as a function of the bubble radius is very well reproduced
 425 with the numerical results.

426 After two hours, the bubble size distribution does not change significantly. It is
 427 noteworthy to see that the numerical method allows to reproduce the probability density
 428 function. These results underline that the numerical method developed in this work is
 429 useful to describe the dynamics of bubble undergoing coalescence.

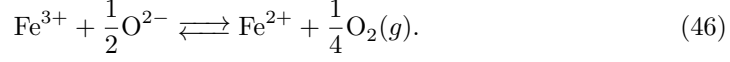
430 4.2. Fining process during the glass melting

431 Fining process is the limiting step in glass melting. As already pinpointed in section
 432 1, the bubble removal in industrial plant is strongly enabled by the addition of “fining
 433 agents”. Hujová and Vernerová [57, 58] did a review of this mechanism in which the
 434 various fining agents are presented. Since the bubble removal is mainly driven by the
 435 bubble rising, the addition of chemical species dissolving gas when the temperature in-
 436 creases leads to a bubble growth. Moreover, the increase of temperature decreases the
 437 viscosity leading to an enhancement of the bubble rising velocity. The effect of sodium
 438 sulfate introduced in raw materials as Na_2SO_4 is studied in this subsection. According
 439 to Chopinet et al. [59], the following chemical reaction

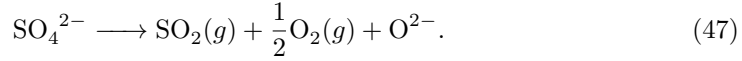


440 is involved with “g” gas species. This last reaction is observed when the glass forming
 441 liquid is enough oxidized. For soda-lime-silicate glasses, the oxidation-reduction state
 442 is controlled by the quantity of the molecular oxygen, O_2 , dissolved in the liquid. It
 443 depends on the redox state of the iron, the main transition metal found in industrial

444 glasses. The oxidation-reduction is then controlled by



445 Equation (45) can be also written in terms of ionic species as follows [59]



446 Knowing the redox state of the iron defined by

$$\mathcal{R}_{\text{Fe}} = \frac{C_{\text{Fe}^{2+}}^l}{C_{\text{Fe}}^l}, \quad (48)$$

447 the oxygen concentration, in mol/m³, dissolved in the glass forming liquid is then deter-
448 mined by

$$C_{\text{O}_2}^l = \left[\frac{(1 - \mathcal{R}_{\text{Fe}})K_{\text{Fe}}}{\mathcal{R}_{\text{Fe}}} \right]^4, \quad (49)$$

449 in which K_{Fe} is the equilibrium constant of the chemical reaction (46). In (48), $C_{\text{Fe}^{2+}}^l$ is
450 the molar concentration of Fe^{2+} and C_{Fe}^l is the total molar concentration of iron equal
451 to $C_{\text{Fe}^{2+}}^l + C_{\text{Fe}^{3+}}^l$, assumed constant all over the time.

452 From the reaction equilibrium of (47), the concentration of SO_2 dissolved in the liquid
453 is given by

$$C_{\text{SO}_2}^l = \frac{C_{\text{S}}^l K_{\text{S}}}{K_{\text{S}} + \sqrt{C_{\text{O}_2}^l}}, \quad (50)$$

454 in which K_{S} is the equilibrium constant of the reaction (47) and C_{S}^l is the total amount
455 of sulfur introduced in the liquid.

456 Beside SO_2 and O_2 species, the nitrogen and carbon dioxide are generally dissolved
457 in glass forming liquid. Since these two species come from the combustion atmosphere
458 above the liquid bath and also from the carbon release of raw materials, the amount of
459 N_2 and CO_2 dissolved in the glass forming liquid can be simply estimated by knowing
460 the partial pressure in atmosphere above the glass bath [60]. This means that $C_{\text{N}_2}^l$ and
461 $C_{\text{CO}_2}^l$ are given by

$$C_{\text{N}_2}^l = \mathcal{L}_{\text{N}_2} P_{\text{N}_2}, \quad (51)$$

$$C_{\text{CO}_2}^l = \mathcal{L}_{\text{CO}_2} P_{\text{CO}_2}. \quad (52)$$

462 One of the first contributions devoted to a quantitative analysis of the fining process
463 has been done by Bastick [6]. He showed that the number of bubbles decreases expo-

T (°C)	$C_{\text{SO}_2}^l$ (mol/m ³)	$C_{\text{O}_2}^l$ (mol/m ³)	$C_{\text{N}_2}^l$ (mol/m ³)	$C_{\text{CO}_2}^l$ (mol/m ³)
1320	8.05	1.35×10^{-3}	1.24×10^{-2}	3.89×10^{-2}
1370	7.27	4.92×10^{-3}	1.41×10^{-2}	3.66×10^{-2}
1420	6.59	1.66×10^{-1}	1.58×10^{-2}	3.46×10^{-2}

Table 3: Molar concentration of gas species dissolved in a window glass for three temperatures.

464 nentially with time. The rate of bubble release increases with temperature but more
465 quickly than expected from the effects of temperature on bubble size and viscosity. The
466 numerical computations are applied to the equivalent situation studied by Bastick [6].
467 There are done for a window glass with 0.1 wt% of iron and a redox state equal to 0.23.
468 The density is equal to 2350 kg/m³ and the viscosity are given by

$$\eta(T) = 1.95 \cdot 10^{-3} \exp\left(\frac{9855.06}{T - 539.15}\right), \quad (53)$$

469 with T in Kelvin. The total amount of sulfur is set equal to 0.39 wt%. Partial pressure of
470 N₂ and CO₂ are determined considering a combustion with air and natural gas. Equilib-
471 rium constants of reactions (46) and (47) and Henry coefficients are given in Appendix
472 A. The initial molar concentrations for SO₂, O₂, N₂ and CO₂ determined with the above
473 developments are reported in Table 3 for three temperatures considered in [6].

474 The numerical application considers a bubble population dispersed in a crucible ob-
475 tained by the melting of raw materials or cullet [6]. The initial bubble density is set equal
476 to 2×10^9 m⁻³. Initially, the bubble size distribution is log-normal, see eq. (41), with
477 $\sigma = 0.434$ and $\mu = -9.33$ given in meter. The initial volume fraction is equal to 1.35 %
478 and the dimensionless parameter K_0 is equal to 2.2. Initially, bubbles are assumed to be
479 composed of air, i.e. 21 % of O₂ and 79 % of N₂. The bubble population is described by
480 taken N equal to 3.

481 Figure 6 depicts the zeroth order moment corresponding to the bubble density nor-
482 malized by the initial value. The solid lines are obtained with the mass transfer. The
483 dashed lines report the numerical results without mass transfer. The experimental results
484 obtained by Bastick [6] have been provided in Figure 6 in solid circles. Colors are the
485 same for all data. The absence of the mass transfer underestimates the bubble release. In
486 dimensionless form, the behavior without mass transfer is completely similar for all tem-
487 peratures. When the mass transfer is introduced, the bubble release enhances in large
488 proportion. For both temperatures, the bubble density decreases quasi-exponentially.
489 The bubble release is mainly driven by the rising of bubble and their escape from the
490 free surface of the glass bath. If the increase of the bubble release would be due to the
491 only viscosity, the behavior of μ_0 should be the same for both temperatures due to the

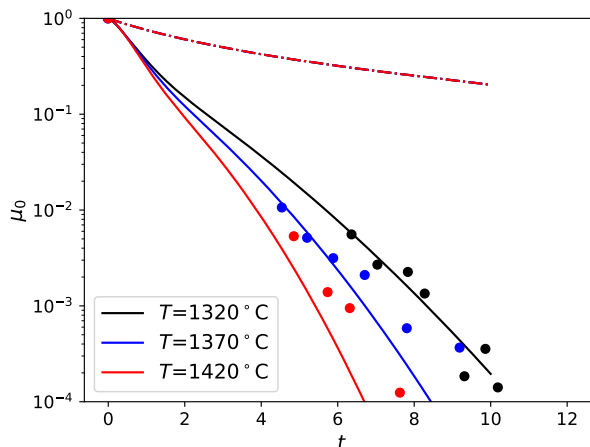


Figure 6: μ_0 as a function of dimensionless time for $T=1320$, 1370 and 1420 °C. Solid lines are obtained with mass transfer while dashed lines are determined without mass transfer. Experimental results obtained by Bastick [6] are plotted with solid circles.

492 normalization of time by the residence time of bubble with a radius a_0 . Globally, the
 493 agreement with the experimental data of Bastick [6] is satisfying even if the numerical
 494 computation predicts a larger rate of decrease for T equal to 1370 and 1420 °C. Note
 495 that the experimental conditions of Bastick [6] have not clearly known. Few of data have
 496 been estimated to do the computations. The numerical computations reproduce well the
 497 fact that the bubble release rate increases faster that the temperature should be done.
 498 The addition of fining agent enhances the bubble release during the glass melting.

499 The Sauter mean radius determined as follows

$$r_{32} = \frac{\mu_3}{\mu_2} \quad (54)$$

500 is plotted as a function of time in Figure 7 for the three temperatures used in the nu-
 501 merical computations. It is noteworthy to see a non-monotonic behavior of r_{32} for both
 502 temperatures. At the early times, the growth rate is quasi similar for all temperatures.
 503 The maximum of bubble size differs with the temperature. The increase of the temper-
 504 ature leads to an increase of the Sauter mean radius. After a decrease of bubble size, an
 505 uniform growth rate is observed for a dimensionless time larger than 3. The growth rate
 506 is larger and larger when the temperature increases. For the smallest temperature, the
 507 Sauter mean radius is only 60% larger than in the initial condition while for the largest
 508 temperature, the bubble size is multiplied by a factor of order 2.17 to the initial value.

509 Figure 8 depicts the size-conditioned molar fraction of the four gas species for the
 510 three values of α . Only results obtained for $T=1320$ °C are reported in Figure 8 since

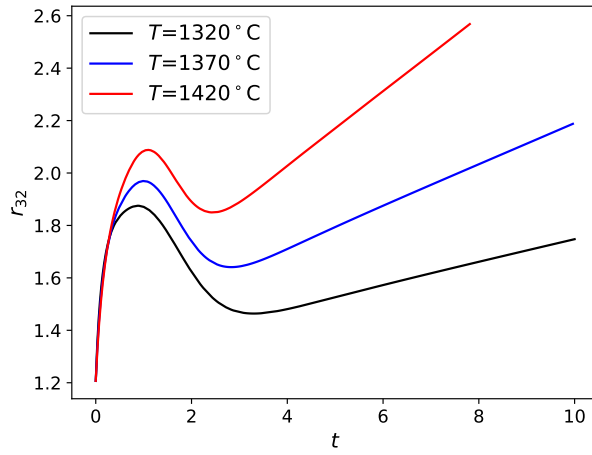


Figure 7: r_{32} as a function of dimensionless time for $T=1320, 1370$ and 1420 °C.

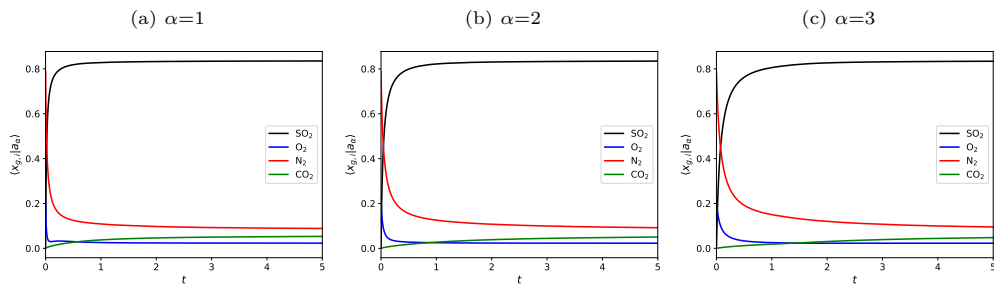


Figure 8: $\langle x_{g,i} \rangle|a_{\alpha}$ as function of dimensionless time at $T=1320$ °C for the four gas species and for the three classes.

511 the behavior of the molar fractions does not significantly change with the temperature.
512 Initially composed by air, the bubble composition changes quickly. Nitrogen and oxygen
513 are replaced by SO_2 gas species which is the most dissolved species. The mass transfer
514 of SO_2 is very efficient due to a large value of the driver force at early stage. At long
515 times, CO_2 becomes more significant than O_2 . The final composition of bubbles is
516 mainly given by SO_2 , N_2 and CO_2 . This result is in agreement with the simpler model
517 developed in [26] for unique bubble initially composed by oxygen. This behavior on the
518 bubble composition underlines that the dynamics of gas species differs for one species
519 to another. The important factor in the mass transfer is the $\mathcal{H}_i \text{Fo}_i$ corresponding to
520 a gas permeability. For SO_2 , O_2 , N_2 and CO_2 , these products are equal to 3.52, 3.76,
521 5.27×10^{-2} and 1.44×10^{-1} respectively. The change of composition is mainly due to
522 the mass transfer of SO_2 and O_2 species. Even if the molar fraction of N_2 decreases in
523 large proportion it is mainly due to the migration of SO_2 .

524 Figure 9 presents the temporal behavior of the molar fraction of the four species
525 dissolved in the glass forming liquid. Results obtained at the three temperatures are
526 provided. Globally, the composition of dissolved gas species changes due to mass transfer
527 from the liquid to bubble population. Apart from O_2 species, the dissolved gas species
528 decrease with the time. For O_2 species, the non-monotonic behavior is due to the mass
529 transfer of bubbles rich in oxygen at short times.

530 These results show the complex coupling between the two phases. As expected the
531 bubble population can play important role in the chemistry of the liquid. The model
532 developed in this work is able to quantify the mass transfer and the bubble release.

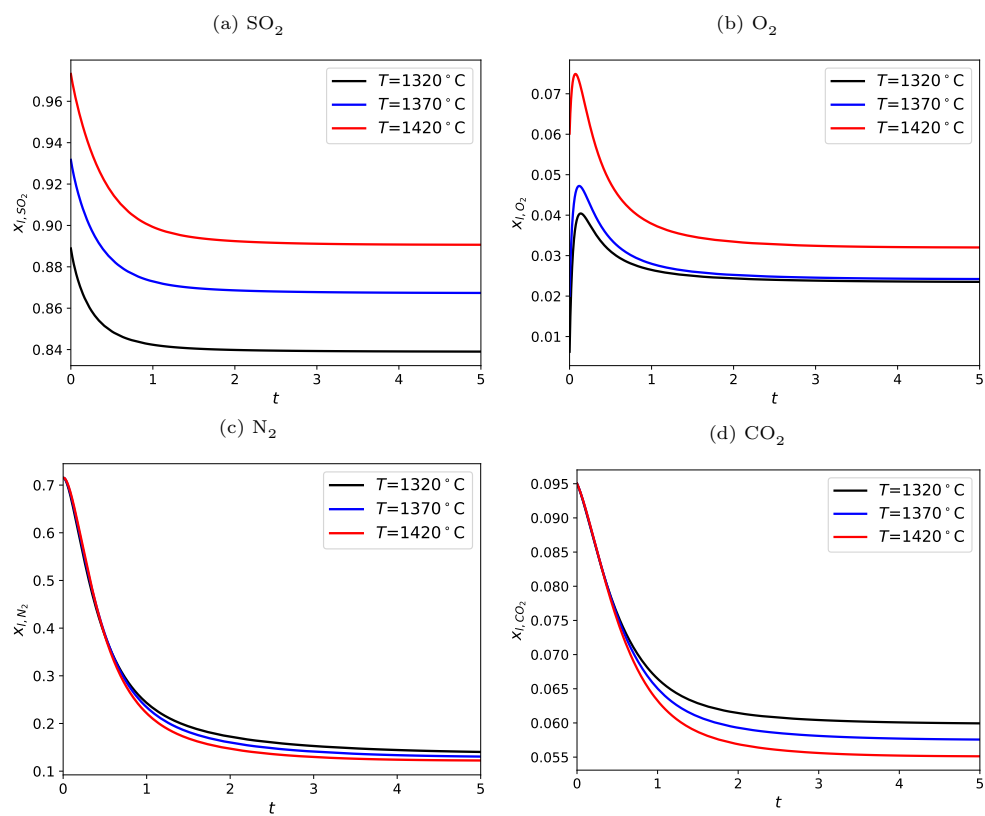


Figure 9: $x_{l,i}$ as function of dimensionless time for the three temperatures.

533 5. Synthesis and perspectives

534 To see the relevance of the bubble coalescence after the glass bead melting and the
535 fining agents on the mass transfer, an original theoretical model based on a popula-
536 tion balance equation is developed. Both mass transfer and coalescence are accounted
537 for. To solve numerically the population balance equation, a direct quadrature method
538 of moments (DQMOM) has been implemented. The numerical method is applied to
539 experiments achieved by Pereira et al. [8] and by Bastick [6].

540 According to Pereira et al. [8], it was observed that the bubble density decreases
541 strongly at short time. Using a coalescence kernel due to the relative rising of bubble,
542 the numerical results well reproduce the experimental behavior. This underlines that the
543 coalescence, as suggested by Cable [9], is the main mechanism of the bubble dynamics
544 in a glass forming liquid. From the numerical results, it is possible to quantify this
545 mechanism. The coalescence becomes significant when the bubble density is larger than
546 10^2 cm^{-3} or in other words, when the mean distance between inclusions gets shorter than
547 1 mm. Apart from the effect of coalescence, both experimental and numerical predictions
548 allow to highlight that the bubble size distribution follows a log-normal law. This result
549 already underlined by Boloré et al. [7] can be useful to follow the bubble dynamics in
550 CFD software. The experimental data provided here can be used to determine the initial
551 bubble size distribution.

552 The application of the numerical model in the case driven by the mass transfer is also
553 efficient. The faster bubble release mentioned by Cable [10] is reproduced and explained.
554 It is mainly due to the change of the glass chemistry with the temperature. The increase
555 of gas release dissolved in the glass forming liquid is the most important phenomena
556 explaining the bubble release. The important feature of the model developed in this
557 work is the coupling with the liquid phase leading to the modification of the chemistry
558 of the liquid.

559 The DQMOM method developed for this work allow to describe the mass transfer by
560 writing balance equation of each molar fraction of relevant gas species dissolved in the
561 liquid. As already presented in [24], it is possible to couple the bubble dynamics with
562 the chemistry of the glass forming liquid. The future step is to develop this model in
563 CFD software and applied it to furnace design. As it is well documented in the textbook
564 of Marchisio and fox [14], DQMOM fails when it is applied to multidimensional cases.
565 The conditional quadrature method of moments proposed by Yuan and Fox [61] could
566 be a relevant choice to extend the work presented here. This work is a main issue since
567 both two-phase flow and the coupling with the glass chemistry are poorly described in
568 existing CFD tools to design glass furnaces.

569 The numerical software developed for this work is accessible following the link [DQ-](#)

570 MOM.

571 Appendix A. Numerical parameters used in the numerical computations

572 Appendix A.1. Henry coefficients

573 The solubility of a gas species i is written as a function of the temperature T as
574 follows

$$\mathcal{L}_i = A_i^{\text{sol}} \exp\left(\frac{B_i^{\text{sol}}}{T}\right). \quad (\text{A.1})$$

575 The constants A_i^{sol} and B_i^{sol} to determine solubilities of the four gas species have been
576 taken from Beerkens [60] for the pressure in Pa and the molar concentration in mol/m³.
577 Table A.4 gathers values for the four gas species used in this work.

Species	O ₂	SO ₂	CO ₂	N ₂
A_i^{sol} (mol/m ³ /Pa)	1.37×10^{-4}	6.44×10^{-7}	5.6×10^{-7}	1.1×10^{-5}
B_i^{sol} (K)	-6633	7860	3120	-6633

Table A.4: Values of A_i^{sol} and B_i^{sol} used to compute the Henry coefficient given by eq. (A.1) according to [60].

578 Appendix A.2. Diffusion coefficients

579 The diffusion coefficients of each species are determined as a function of temperature
580 following the relation

$$\mathcal{D}_i = A_i^{\text{diff}} \exp\left(-\frac{B_i^{\text{diff}}}{T}\right), \quad (\text{A.2})$$

581 for which A_i^{diff} and B_i^{diff} are provided in Table A.5.

Species	O ₂	SO ₂	CO ₂	N ₂
$A_{G_i}^{\text{diff}}$ (m ² /s)	4.2×10^{-3}	4.45×10^{-7}	1.92×10^{-5}	4.3×10^{-5}
$B_{G_i}^{\text{diff}}$ (K)	26 646	15 360	21 516	19 364

Table A.5: Values of A_i^{diff} and B_i^{diff} used to compute the coefficient coefficient given by eq. (A.2) according to [60].

582 Appendix A.3. Equilibrium constants

583 According to Kondepudi and Prigogine [62], the equilibrium constant is written as
584 follows

$$K_r = \exp\left(-\frac{\Delta G_r}{RT}\right), \quad (\text{A.3})$$

585 with the Gibbs energy given by

$$\Delta G_r = \Delta H_r - T\Delta S_r. \quad (\text{A.4})$$

586 The numerical values of the enthalpy and entropy of cerium reaction, (42), iron re-
587 action, (46), and sulfur reaction, (47), are reported in Table A.6. Equilibrium constants
588 are written with the molar concentration of O₂. Consequently, the values of ΔH_r and
589 ΔS_r provided in Table A.6 take into account the oxygen solubility.

Reaction	Ce	Fe	S
ΔH_r (kJ mol ⁻¹)	77.5	141	233
ΔS_r (J mol ⁻¹ K ⁻¹)	51.06	64.56	97.58

Table A.6: Enthalpy and entropy of Ce reaction, (42), from [55] and reactions (46) and (47) according to [60].

590 References

- 591 [1] H. M. Gonnermann and M. Manga. The Fluid Mechanics Inside a Volcano. *Annu. Rev. Fluid*
592 *Mech.*, 39:321–356, 2007.
- 593 [2] G. Liger-Belair. The Physics and Chemistry behind the Bubbling Properties of Champagne and
594 Sparkling Wines: A State-of-the-Art Review. *J. Agric. Food. Chem.*, 53(8):2788–2802, 2005.
- 595 [3] S. Seetharaman, A. McLean, R. Guthrie, and S. Sridhar, editors. *Treatise on process metallurgy*,
596 volume 2. Elsevier, 2014.
- 597 [4] M. Ishii and T. Hibiki. *Thermo-fluid Dynamics of Two-phase Flow*. Springer, 2011.
- 598 [5] J. E. Shelby. *Introduction to glass science and technology*. The Royal Society of Chemistry, Cam-
599 bridge, third edition, 2015.
- 600 [6] R. E. Bastick. Laboratory experiments on the refining of glass. In *Symposium sur l'affinage du*
601 *verre*, pages 127–138, Paris, 1956.
- 602 [7] D. Boloré, M. Gibilaro, L. Massot, P. Chamelot, E. Cid, O. Masbernat, and F. Pigeonneau. X-ray
603 imaging of a high temperature furnace applied to glass melting. *J. Am. Ceram. Soc.*, 103:979–992,
604 2020.
- 605 [8] L. Pereira, O. Podda, B. Fayard, A. Laplace, and F. Pigeonneau. Experimental study of bubble
606 formation in a glass-forming liquid doped with cerium oxide. *J. Am. Ceram. Soc.*, 103:2453–2462,
607 2020.
- 608 [9] M. Cable. A study of refining. Part 2: Mechanisms of refining. *Glass Technol.*, 2:60–70, 1961.
- 609 [10] M. Cable. A century of developments in glassmelting research. *J. Amer. Ceram. Soc.*, 81:1083–1094,
610 1998.
- 611 [11] A. D. Randolph and M. A. Larson. Transient and steady state size distributions in continuous
612 mixed suspension crystallizers. *AIChE J.*, 8(5):639–645, 1962.
- 613 [12] H. M. Hulburt and S. Katz. Some problems in particles technology. *Chem. Eng. Sci.*, 19:555–574,
614 1964.
- 615 [13] D. Ramkrishna. *Population balances. Theory and application to particulate systems in engineering*.
616 Academic Press, San Diego, 2000.

- 617 [14] D. L. Marchisio and R. O. Fox. *Computational models for polydisperse particulate and multiphase*
618 *systems*. Cambridge University Press, 2013.
- 619 [15] A. Ungan, W. H. Turner, and R. Viskanta. Effect of gas bubbles on three-dimensional circulation
620 in a glass melting tank. *Glastechn. Ber.*, 56K:125–129, 1983.
- 621 [16] A. Ungan, R. U. Payli, and B. Balkanli. Numerical model of polydispersed silica grain dissolution
622 in glass melting furnaces. *J. Am. Ceram. Soc.*, 77:1921–1927, 1994.
- 623 [17] T. Roi, O. Seidel, G. Nölle, and D. Höhne. Modeling of the bubble population in glass melt. *Glass*
624 *Sci. Technol.*, 67:263–271, 1994.
- 625 [18] B. Balkanli and A. Ungan. Numerical simulation of bubble behaviour in glass melting tanks. Part
626 4. Bubble number density distribution. *Glass Technol.*, 37:164–168, 1996.
- 627 [19] A. Bensberg and C. Breitbach. Bubble continuum model. In *Advances in Fusion and Processing*
628 *of Glass III*, Ohio, 2004.
- 629 [20] L. Pilon, A. G. Fedorov, D. Ramkrishna, and R. Viskanta. Bubble transport in three-dimensional
630 laminar gravity-driven flow – mathematical formulation. *J. Non-Cryst. Solids*, 336:71–83, 2004.
- 631 [21] L. Pilon and R. Viskanta. Bubble transport in three-dimensional laminar gravity-driven flow –
632 numerical results. *J. Non-Cryst. Solids*, 336:84–95, 2004.
- 633 [22] L. Pilon and R. Viskanta. Modified method of characteristics for solving population balance equa-
634 tions. *Int. J. Num. Meth. Fluids*, 42:1211–1236, 2003.
- 635 [23] K. Oda and M. Kaminoyama. Mathematical model of bubble number density in glass tank furnace.
636 *J. Ceram. Soc. Jpn.*, 117(1366):736–741, 2009.
- 637 [24] F. Pigeonneau. Coupled modelling of redox reactions and glass melt fining processes. *Glass Technol.:*
638 *Eur. J. Glass Sci. Technol. A*, 48(2):66–72, 2007.
- 639 [25] J. I. Ramos. Behavior of multicomponent gas bubbles in glass melts. *J. Am. Ceram. Soc.*, 69:149–
640 154, 1986.
- 641 [26] F. Pigeonneau. Mechanism of mass transfer between a bubble initially composed of oxygen and
642 molten glass. *Int. J. Heat Mass Transfer*, 54:1448–1455, 2011.
- 643 [27] S.-M. Yang and L. G. Leal. A note on memory-integral contributions to the force on an accelerating
644 spherical drop at low reynolds number. *Phys. Fluids A*, 3(7):1822–1824, 1991.
- 645 [28] J. Magnaudet and D. Legendre. The viscous drag force on a spherical bubble with a time-dependent
646 radius. *Phys. Fluids*, 10(3):550–554, 1998.
- 647 [29] J. Hadamard. Mouvement permanent lent d’une sphère liquide et visqueuse dans un liquide
648 visqueux. *C. R. Acad. Sci. Paris*, 152:1735–1738, 1911.
- 649 [30] W. Rybczynski. Über die fortschreitende bewegung einer flussigen kugel in einem zähen medium.
650 *Bull. de l’Acad. des Sci. de Cracovie, série A*, 1:40–46, 1911.
- 651 [31] M. S. Plesset and A. Prosperetti. Bubble dynamics and cavitation. *Annu. Rev. Fluid Mech.*,
652 9(1):145–185, Jan 1977.
- 653 [32] V. G. Levich. *Physicochemical hydrodynamics*. Prentice Hall, Englewood Cliffs, N.J., 1962.
- 654 [33] R. Clift, J. R. Grace, and M. E. Weber. *Bubbles, Drops, and Particles*. Academic Press, New York,
655 1978.
- 656 [34] F. Pigeonneau, D. Martin, and O. Mario. Shrinkage of oxygen bubble rising in a molten glass.
657 *Chem. Eng. Sci.*, 65:3158–3168, 2010.
- 658 [35] R. Sander. Compilation of Henry’s law constants (version 4.0) for water as solvent. *Atmos. Chem.*
659 *Phys.*, 15(8):4399–4981, 2015.
- 660 [36] R. Fan, D. L. Marchisio, and R. O. Fox. Application of the direct quadrature method of moments
661 to polydisperse gas-solid fluidized beds. *Powder Technol.*, 139:7–20, 2004.
- 662 [37] Y. Liao and D. Lucas. A literature review on mechanisms and models for the coalescence process
663 of fluid particles. *Chem. Eng. Sci.*, 65(10):2851–2864, 2010.

- 664 [38] X. Zhang and R. H. Davis. The rate of collisions due to brownian or gravitational motion of small
665 drops. *J. Fluid Mech.*, 230:479–504, 1991.
- 666 [39] A. Z. Zinchenko. Calculation of the effectiveness of gravitational coagulation of drops with allowance
667 for internal circulation. *Prikl. Matem. Mekhan.*, 46:72–82, 1982.
- 668 [40] A. Kovetz and B. Olund. The effect of coalescence and condensation on rain formation in a cloud
669 of finite vertical extent. *J. Atmos. Sci.*, 26(5):1060–1065, 1969.
- 670 [41] F. Pigeonneau and F. Feuillebois. Collision and size evolution of drops in homogeneous isotropic
671 turbulence. *J. Aerosol Sci.*, 29:S1279–S1280, 1998.
- 672 [42] F. Gelbard and J. H. Seinfeld. Numerical solution of the dynamic equation for particulate systems.
673 *J. Comput. Phys.*, 28(3):357–375, 1978.
- 674 [43] D. Ramkrishna. Solution of population balance equations. *Chem. Eng. Sci.*, 26:1134–1136, 1971.
- 675 [44] D. Ramkrishna. The status of population balances. *Rev. Chem. Eng.*, 3(1):49–95, 1985.
- 676 [45] H. M. Hulburt and T. Akiyama. Liouville equations for agglomeration and dispersion processes. *I.*
677 *© E. C. Fundamentals*, 8-2:319–324, 1969.
- 678 [46] D. L. Marchisio and R. O. Fox. Solution of population balance equations using the direct quadrature
679 method of moments. *J. Aerosol Sci.*, 36:43–73, 2005.
- 680 [47] R. G. Gordon. Error bounds in equilibrium statistical mechanics. *J. Math. Phys.*, 9(5):655–663,
681 1968.
- 682 [48] J. C. Wheeler. Modified moments and gaussian quadratures. *Rocky Mt. J. Math.*, 4(2):287–296,
683 1974.
- 684 [49] D. L. Marchisio, R. D. Vigil, and R. O. Fox. Implementation of the quadrature method of moments
685 in CFD codes for aggregation-breakage problems. *Chem. Eng. Sci.*, 58:3337–3351, 2003.
- 686 [50] L. Pereira, M. Vernerová, J. Kloužek, A. Laplace, and F. Pigeonneau. Experimental and numerical
687 studies of an oxygen single-bubble shrinkage in a borosilicate melt doped with cerium oxide. *J. Am.*
688 *Ceram. Soc.*, 103:6736–6745, 2020.
- 689 [51] H. Scholze. *Glass. Nature, Structures and Properties*. Springer-Verlag, Berlin, 1990.
- 690 [52] A. K. Varshneya and J. C. Mauro. *Fundamentals of Inorganic Glasses*. Elsevier, third edition,
691 2019.
- 692 [53] A. Baddeley and E. B. Vedel Jensen. *Stereology for statisticians*. Chapman and Hall/CRC, 2005.
- 693 [54] N. Reboul, E. Vincens, and B. Cambou. A statistical analysis of void size distribution in a simulated
694 narrowly graded packing of spheres. *Granular Matter*, 10(6):457–468, 2008.
- 695 [55] O. Pinet, J. Phalippou, and C. Di Nardo. Modeling the redox equilibrium of the Ce^{4+}/Ce^{3+} couple
696 in silicate glass by voltammetry. *J. Non-Cryst. Solids*, 352(50-51):5382–5390, 2006.
- 697 [56] M. Ungarish. *Hydrodynamics of suspensions*. Springer-Verlag, Berlin, 1993.
- 698 [57] M. Hujová and M. Vernerová. Influence of fining agents in glass melting: A review, part 1. *Ceramics-*
699 *Silikáty*, 61(2):119–126, 2017.
- 700 [58] M. Hujová and M. Vernerová. Influence of fining agents in glass melting: A review, part 2. *Ceramics-*
701 *Silikáty*, 61(3):202–208, 2017.
- 702 [59] M.-H. Chopinet, D. Lizarazu, and C. Rocanière. L’importance des phénomènes d’oxydo-réduction
703 dans le verre. *C. R. Chimie*, 5(12):939–949, 2002.
- 704 [60] R. G. C. Beerkens. Analysis of advanced and fast fining processes for glass melts. In *Advances in*
705 *Fusion and Processing of Glass III*, pages 3–24. American Ceramic Society, New York, 2004.
- 706 [61] C. Yuan and R. O. Fox. Conditional quadrature method of moments for kinetic equations. *J.*
707 *Comput. Phys.*, 230(22):8216–8246, 2011.
- 708 [62] D. Kondepudi and I. Prigogine. *Modern Thermodynamics: From Heat Engines to Dissipative*
709 *Structures*. John Wiley & Sons, New York, 2nd edition, 2015.